

Double and Quadruple Flat Bands tuned by Alternative magnetic Fluxes in Twisted Bilayer Graphene

Congcong Le,¹ Qiang Zhang,² Cui Fan,^{2,3} Xianxin Wu,^{4,*} and Ching-Kai Chiu^{1,†}

¹*RIKEN Interdisciplinary Theoretical and Mathematical Sciences (iTHEMS), Wako, Saitama 351-0198, Japan*

²*Institute of Physics, Chinese Academy of Sciences, Beijing 100190, China*

³*University of Chinese Academy of Sciences, Beijing 100049, China*

⁴*CAS Key Laboratory of Theoretical Physics, Institute of Theoretical Physics, Chinese Academy of Sciences, Beijing 100190, China*

(Dated: October 26, 2022)

Twisted bilayer graphene (TBG) can host the moiré energy flat bands with two-fold degeneracy serving as a fruitful playground for strong correlations and topological phases. However, the number of degeneracy is not limited to two. Introducing a spatially alternative magnetic field, we report that the induced magnetic phase becomes an additional controllable parameter and leads to the emergence of four-fold degenerate flat bands. This emergence stems from the band inversion at Γ point near the Fermi level with a variation of both twisted angle and magnetic phase. Using holomorphic functions, which explain the origin of the double flat bands in the conventional TBG, we can generate analytical wave functions in the magnetic TBG to show absolutely flat bands with four-fold degeneracy. In contrast, the conventional TBG has only two moiré energy flat bands, and the highly degenerate flat bands in this magnetic platform might bring richer correlation physics.

PACS numbers: 73.43.-f, 73.20.-r, 71.20.-b

Introduction – Moiré twistrionics is the study of the electrical properties of two-dimensional (2D) multilayers with twists and has attracted enormous attention in contemporary research[1–10]. In particular, twisted bilayer graphene (TBG) is one of the prominent platforms. When the twisted angle is adjusted to be magic values, the low energy electronic structure stemming from the Dirac cones evolves to flat bands in a direct gap. Moreover, since the flat-band states are delocalized[11, 12], the emergence of the electron-electron interaction fosters tunable strong-correlation phenomena, such as correlated insulating states[2, 5, 13–17], unconventional high temperature superconductivity[3, 5, 17–19], quantum anomalous Hall effect[20–22].

The origin of magic angles leading to two-fold degenerate flat bands has been one of the main interests in mathematics and physics communities. Recently, Vishwanath’s group [23] studied the fundamental continuum model of TBG preserving chiral symmetry and mathematically showed the entire lowest band is perfectly flat due to holomorphic functions. On the other hand, Zworski’s group used the spectral of a compact non-Hermitian Birman-Schwinger operator to obtain the series of magic angles for absolutely two-fold degenerate flat bands [24, 25]. However, beyond the two-fold degeneracy, is it possible to realize higher degeneracy of the flat bands by adjusting another physical parameter?

To seek the high degeneracy of the flat bands, we introduce a magnetic field that spatially alternates directions inside each monolayer graphene as illustrated in Fig. 1(a). Under the effect of the alternative magnetic field, like Haldane’s model[26], the nearest-neighbor hopping in the monolayer graphene can acquire an additional magnetic phase φ as an additional physical parameter. While in the conventional

TBG, the magic angles correspond to the real eigenvalues of the Birman-Schwinger operator, the phase φ expands the flat bands’ solutions to the complex eigenvalues of the same operator. Remarkably, a variety of the complex eigenvalues manifest four-fold absolutely flat bands. Our work demonstrates that the magnetic phase is a unique tuning parameter to tailor the electronic structure in moiré twistrionics, which can significantly enrich the correlation physics. Let us start with the continuum model of the magnetic TBG for the details.

Model–To be specific, we consider monolayer graphene with alternative magnetic fluxes in each triangle inside a hexagonal plaquette, as shown in Fig.1(a). The blue (\odot) and yellow (\otimes) triangles denote outward-to-the-plane and inward-to-the-plane fluxes, and the total flux through each hexagonal plaquette vanishes. With a Peierls substitution, the nearest-neighbor hopping acquires a magnetic phase φ . The Dirac Hamiltonian in the real space gains an additional phase and reads (see Supplemental Material(SM) for details)

$$h_D^\varphi(\mathbf{r}) = -v_0 \begin{pmatrix} 0 & e^{-i\varphi} 2\bar{\partial} \\ e^{i\varphi} 2\bar{\partial} & 0 \end{pmatrix}, \quad (1)$$

with $\bar{\partial} = \frac{1}{2i}(\partial_x + i\partial_y)$ and Fermi velocity v_0 . The standard Dirac Hamiltonian is restored for monolayer graphene in the absence of magnetic flux ($\varphi = 0$). Then, as shown in Fig.1(b), we introduce a twist with angle θ between these two graphene layers. We use the basis of $\Phi(\mathbf{r}) = (e^{i\frac{\varphi}{2}} \psi_A^t, e^{i\frac{\varphi}{2}} \psi_A^b, e^{-i\frac{\varphi}{2}} \chi_B^t, e^{-i\frac{\varphi}{2}} \chi_B^b)^\top$, which absorbs the magnetic phase, where t/b denotes the top/bottom graphene layers and A/B is the sublattice index. The chirally symmetric continuum model of TBG with alternating fluxes can be written as

$$H^\varphi(\mathbf{r}) = \begin{pmatrix} 0 & D^{\varphi*}(-\mathbf{r}) \\ D^\varphi(\mathbf{r}) & 0 \end{pmatrix}, \quad (2)$$

$$D^\varphi(\mathbf{r}) = \begin{pmatrix} 2\bar{\partial} & e^{i(\varphi+\beta)} \alpha_0 U(\mathbf{r}) \\ e^{i(\varphi-\beta)} \alpha_0 U(-\mathbf{r}) & 2\bar{\partial} \end{pmatrix}, \quad (3)$$

*Electronic address: xxwu@itp.ac.cn

†Electronic address: ching-kai.chiu@riken.jp

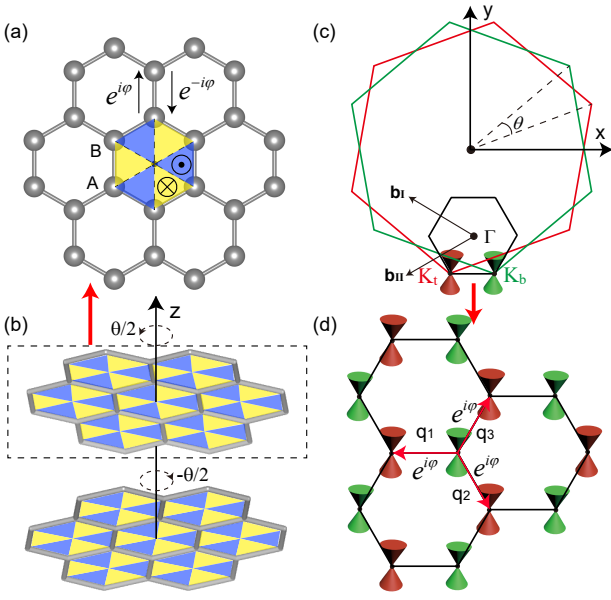


FIG. 1: (color online) (a) Distribution of periodic local magnetic fluxes in hexagonal plaquette of monolayer graphene with basis A and B. The blue (\odot) and yellow (\otimes) regions denote outward-to-the-plane and inward-to-the-plane magnetic fluxes, respectively. The magnetic fluxes induces an additional phase φ in the nearest neighbor hoppings. (b) Twisted bilayer graphene with alternative fluxes. (c) The two monolayer Brillouin Zones (BZs) with the twist form a moiré BZ. The red and green hexagons represent the BZs of the bottom and top layers, each rotated by an angle $\pm\theta/2$, and the small black hexagon indicates the moiré BZ with momentum bases $\mathbf{b}_{1/2} = \sqrt{3}k_\theta(-\sqrt{3}/2, \pm 1/2)$. (d) The reciprocal lattice structures. Effectively, the interlayer coupling with the phase φ couple the red and green Dirac cones separately located in the top and bottom Dirac cones.

where $U(\mathbf{r}) = e^{-i\mathbf{q}_1 \cdot \mathbf{r}} + e^{-i\mathbf{q}_2 \cdot \mathbf{r}} e^{i\phi} + e^{-i\mathbf{q}_3 \cdot \mathbf{r}} e^{-i\phi}$ with $\phi = 2\pi/3$. $\mathbf{q}_1 = k_\theta(-1, 0)$, $\mathbf{q}_{2,3} = k_\theta(1/2, \mp\sqrt{3}/2)$ are shown in Fig.1(d) with $k_\theta = 2k_D \sin(\theta/2)$, and $k_D = |\mathbf{K}_{t/b}|$ is Dirac momentum in the monolayer graphene. The above Hamiltonian is characterized by a dimensionless real parameter $\alpha_0 e^{i\beta} = \frac{\omega_{AB}}{v_0 k_\theta}$, where ω_{AB} is the strength of the interlayer coupling with a phase β . Unlike the magnetic phase φ , the global phase β can be gauged away. For simplicity, we define a complex parameter $\alpha(\varphi) \equiv \alpha_0 e^{i\varphi}$. In addition, $H^\varphi(\mathbf{r})$ is off-diagonal as we consider the chiral limit, where we neglect intra-sublattice (AA/BB) interlayer hopping. Since the twisted angle is small, we also neglect the rotation effect on the graphene Dirac Hamiltonian $h_D^\varphi(\mathbf{r})$ [23]. In the momentum space, the Hamiltonian $H^\varphi(\mathbf{r})$ can be illustrated by the network of the two Dirac cones with the extension of the momentum hoppings, where the hopping between the nearest-neighbor momentum sites acquires a phase $e^{i\varphi}$ owing to the alternative fluxes in the monolayers, as shown in Fig.1(c) and (d). This phase plays a pivotal role in generating multi-fold flat bands.

Multi-fold flat bands– We further discuss the conditions of absolutely zero-energy flat bands for the above continuum model. After a gauge transformation $V =$

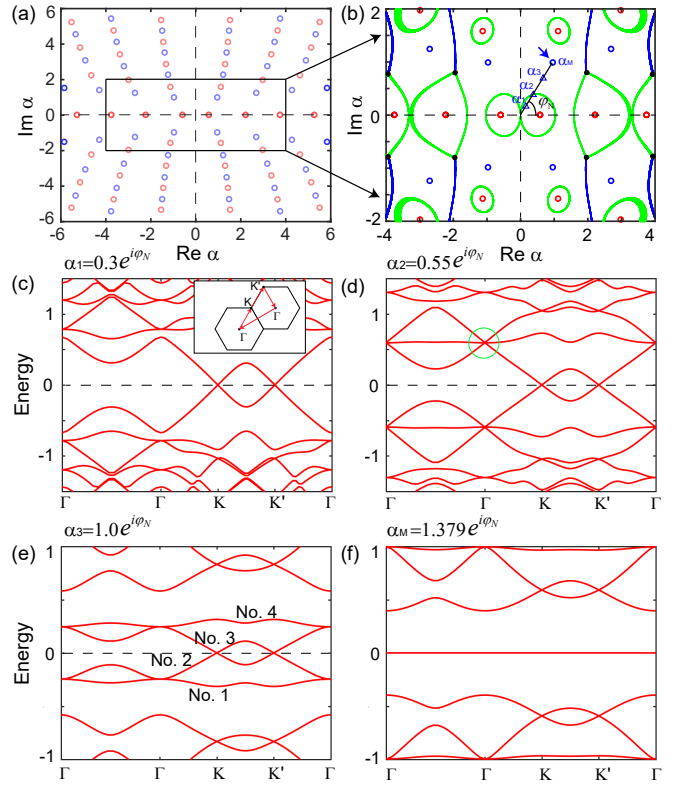


FIG. 2: (color online) (a) The spectra \mathcal{A} shows the magic values of the dimensionless complex parameter α corresponding to double (red) and quadruple (blue) flat bands. (b) The distribution of lowest energy band touching at Γ point in the spectra \mathcal{A} shows that blue, green, and black lines denote band touching with four-fold, three-fold, and five-fold degeneracy, respectively. The band structures of the Hamiltonian $H^\varphi(\mathbf{r})$ with magnetic phase $\varphi_N = 0.254\pi$ in the different α_0 values marked by blue triangle in (b). (c) $\alpha_1 = 0.3e^{i\varphi_N}$, (d) $\alpha_2 = 0.55e^{i\varphi_N}$, (e) $\alpha_3 = 1.0e^{i\varphi_N}$ and (f) $\alpha_M = 1.379e^{i\varphi_N}$, which is the magic value pointed by a blue arrow. The inset in (c) indicates the spectrum path in the moiré BZ. The green circle in (d) denotes band inversion between double degenerate and non-degenerate points at Γ .

$\text{diag}(e^{-i\mathbf{k} \cdot \mathbf{r}}, e^{-i\mathbf{k} \cdot \mathbf{r}})$, the Hamiltonian $H_{\mathbf{k}}^\varphi(\mathbf{r}) = V^\dagger H^\varphi(\mathbf{r}) V$ can be written in term of complex variables,

$$H_{\mathbf{k}}^\varphi(\mathbf{r}) = \begin{pmatrix} 0 & D_{\mathbf{k}}^{\varphi*}(-\mathbf{r}) \\ D_{\mathbf{k}}^\varphi(\mathbf{r}) & 0 \end{pmatrix}, \quad (4)$$

where $D_{\mathbf{k}}^\varphi(\mathbf{r}) \equiv D^\varphi(\mathbf{r}) - \mathbf{k}$ and the momentum \mathbf{k} is defined in moiré BZ. The explicit form of $D_{\mathbf{k}}^\varphi(\mathbf{r})$ is given by

$$D_{\mathbf{k}}^\varphi(\mathbf{r}) = (2\bar{\delta} - \mathbf{k})(I + \alpha(\varphi)T_{\mathbf{k}}), \\ T_{\mathbf{k}} = (2\bar{\delta} - \mathbf{k})^{-1} \begin{pmatrix} 0 & U(\mathbf{r}) \\ U(-\mathbf{r}) & 0 \end{pmatrix}, \quad (5)$$

where $T_{\mathbf{k}}$ ($\mathbf{k} \neq 0$) is the Birman-Schwinger operator [24, 25]. The appearance of absolutely zero-energy flat bands implies that the determinant of Hamiltonian $H_{\mathbf{k}}^\varphi(\mathbf{r})$ is zero for all \mathbf{k} , i.e. $\det(D_{\mathbf{k}}^\varphi(\mathbf{r})) = 0$. Inversely, due to $\det(2\bar{\delta} - \mathbf{k}) \neq 0$, for all non-zero \mathbf{k} the matrix $[I - \alpha(\varphi)T_{\mathbf{k}}]$ should have at least

one zero eigenvalue and for $\mathbf{k} = 0$ two low-energy states are fixed at zero energy. According to Ref.[24, 25], the eigenvalues of $T_{\mathbf{k}}$ are independent of \mathbf{k} and then we can define a spectrum $\mathcal{A} = 1/\text{Spec}(T_{\mathbf{k}})$ and a corresponding two-component eigenstate $\psi_{\mathbf{k}}^0(\mathbf{r})$. Therefore, once the parameter α is tuned to be one of the complex eigenvalues in \mathcal{A} , $D_{\mathbf{k}}^{\varphi}(\mathbf{r})\psi_{\mathbf{k}}^0(\mathbf{r}) = 0$ so that zero-energy flat bands emerge in $H_{\mathbf{k}}^{\varphi}(\mathbf{r})$ and α has a magic value.

In the absence of the alternative magnetic field ($\varphi = 0$), the magic parameters α in the conventional TBG appear recursively on the real axis of spectrum \mathcal{A} [24, 25], as shown in Fig.2(a) and indicate the presence of double flat bands. When the alternative magnetic field is recovered, the magic values of α are expanded to the entire complex plane. The eigenvalues α of spectrum \mathcal{A} exhibit no degeneracy (red circles) and two-fold degeneracy (blue circles), respectively (Fig.2(a)). The non-degenerate and two-fold degenerate eigenvalues correspond to double and quadruple flat bands in magnetic TBG. The reason is that the two-component eigenstate $\psi_{\mathbf{k}}^0(\mathbf{r})$ generates two zero-energy four-component wavefunctions $(\psi_{\mathbf{k}}^{0\top}(\mathbf{r}) \ 0 \ 0)^{\top}$, $(0 \ 0 \ \psi_{\mathbf{k}}^{0\dagger}(-\mathbf{r}))^{\top}$ in $H_{\mathbf{k}}^{\varphi}(\mathbf{r})$ due to $C_{2z}T$ symmetry(See SM). Introducing the alternative magnetic field extends magic parameters to more discrete values and leads to the emergence of the four-fold degenerate flat bands.

The Hamiltonian $H_{\mathbf{k}}^{\varphi}(\mathbf{r})$ preserves the combination symmetry of time-reversal and C_{2z} rotation with operator $C_{2z}T = \tau_x\sigma_0\mathcal{K}$ and chiral symmetry with operator $S = \tau_z\sigma_0$ with sublattice index τ and layer index σ , where T is time reversal operator and \mathcal{K} is the complex conjugation. Furthermore, the SM shows that the low-energy physics preserves rotational symmetries $C_{2x} = \tau_x\sigma_0$ and $C_{2y} = \tau_y\sigma_y$. By acting $C_{2z}T$ symmetry on a non-degenerate 4-component wave function $\Psi_{\mathbf{k}}(\mathbf{r})$, the wavefunction can be economically written by $\Psi_{\mathbf{k}}(\mathbf{r}) = (\psi_{\mathbf{k}}^{\top}(\mathbf{r}) \ \psi_{\mathbf{k}}^{\dagger}(-\mathbf{r}))^{\top}$, where $\psi_{\mathbf{k}}^{\top}(\mathbf{r})$ is the first two component of the wave function. Due to C_{2x} symmetry, the wave function obeys $\psi_{\mathbf{k}}(\mathbf{r}) = \psi_{C_{2x}\mathbf{k}}^*(-C_{2x}\mathbf{r})$; hence, the norm of the wave function $\psi_{\mathbf{k}}(\mathbf{r})$ on C_{2x} -symmetric \mathbf{k} path has C_{2y}^r symmetry in the real space. Similarly, for the combined $C_{2z}T$ and C_{2y} symmetry, the norm of the wave function $\psi_{\mathbf{k}}(\mathbf{r})$ on C_{2y} -symmetric \mathbf{k} path has C_{2x}^r symmetry in the real space. (More details can be found in SM)

To investigate the evolution of the degeneracy in the spectra of the magnetic TBG, we take the complex eigenvalue closest to the origin in Fig.2(b) as a example with magnetic phase $\varphi_N = 0.254\pi$ to demonstrate the changes of the low energy bands. The degeneracy of flat bands is intimately related to the degeneracy of the lowest energy states at Γ in the TBG spectrum. To understand the transition of flat bands with different degeneracies as α varies, we can track the band touch of the low-energy states at Γ , as shown in Fig.2(b). The green (blue) curves represent a three-fold (four-fold) band touching at Γ , resulting in band inversions between one singlet and one doublet (between two doublets). Importantly, the three-fold degeneracy curves (Fig.2(d)) separate the magic parameters α with double and quadruple flat bands. Inside one of these degeneracy loops, two connected bands near zero energy in a direct gap (Fig.2(c)) evolve to double flat bands at

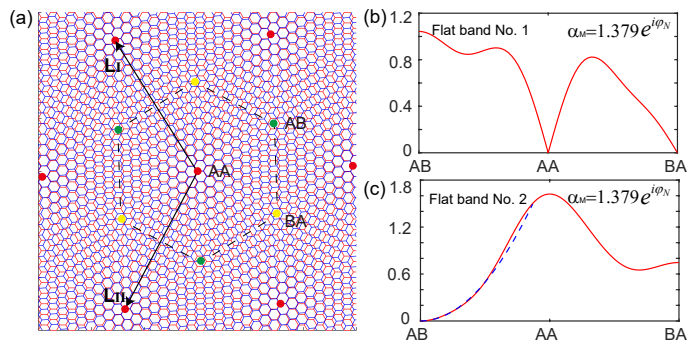


FIG. 3: (color online) (a) Schematic moiré pattern. The red, green and yellow points indicate the AA, AB and BA stacking points, and $\mathbf{L}_{I/II} = 4\pi/3k_{\theta}(-1/2, \pm\sqrt{3}/2)$ are moiré lattice vector. (b) and (c) The norm of the 2-component wave functions $\psi_{\mathbf{K},1/2}(\mathbf{r})$ at \mathbf{K} point for flat bands No.1/2 at the magic $\alpha_M = 1.379e^{i\varphi_N}$. The blue dashed line in (c) represents the fitting of quadratic function.

magic α (red circles). As α crosses a three-fold degeneracy line, the band inversion changes two connected bands to four connected ones in the gap (Fig.2(e)). Outside these degeneracy loops, the four connected bands evolve to quadruple flat bands (Fig.2(f)) at magic α (blue circles), in sharp contrast to the double flat bands in the conventional TBG. In addition, as discussed in the SM, the double and quadruple flat bands are topologically nontrivial with a topological invariant $\mathbb{Z}_2 = 1$.

Origin of quadruple flat bands– In the conventional TBG, the key to rigorously showing the emergence of the two-fold degenerate absolutely-flat bands is that at the magic angles, the zero-energy wave functions at \mathbf{K}/\mathbf{K}' have a linear-dispersion node at BA/AB stacking (in the Moiré unit cell). Using this wavefunction at \mathbf{K} , one generates two eigenfunctions with zero energy at any momentum point [23]. For the magnetic TBG, in the following, we use a similar approach to show the absolute flatness of the four-fold degenerate bands at magic α by identifying the nodes of the wavefunctions at \mathbf{K} and extending this function to the entire Moiré BZ.

To distinguish the quadruple flat bands, consider α slightly away from the magic value (Fig.2(e)). The two lowest bands are labeled by No.1/2 respectively, and the remaining two bands can be generated by chiral symmetry operator $S = \tau_z\sigma_0$. In addition, due to C_2T symmetry, the non-degenerate 4-component wave function $\Psi_{\mathbf{k},i}(\mathbf{r})$ can be expressed by a 2-component vector $\psi_{\mathbf{k},i}(\mathbf{r})$ with band index $i = 1, 2$. At the magic $\alpha_M = 1.379e^{i\varphi_N}$, the norm $[\psi_{\mathbf{K},1/2}^{\dagger}(\mathbf{r})\psi_{\mathbf{K},1/2}(\mathbf{r})]^{1/2}$ shows that for flat band No.1 at \mathbf{K} , two nodes appear at the AA and BA stacking with a dominant linear real-space dependence (Fig.3(b)). Meanwhile, for flat band No.2 at \mathbf{K} , there is only one node at the AB stacking, and the norm exhibits real-space quadratic dependence near it, implying a second order node (Fig.3(c)). These nodal features in sharp contrast to the conventional TBG are the important ingredients for the absolute flatness of the quadruple bands.

To simplify the absolute flatness' problem, we focus on the solution of $D^{\varphi}(\mathbf{r})\psi_{\mathbf{k}}(\mathbf{r}) = 0$ for all \mathbf{k} . Previously, we numerically obtain the two-component wave functions

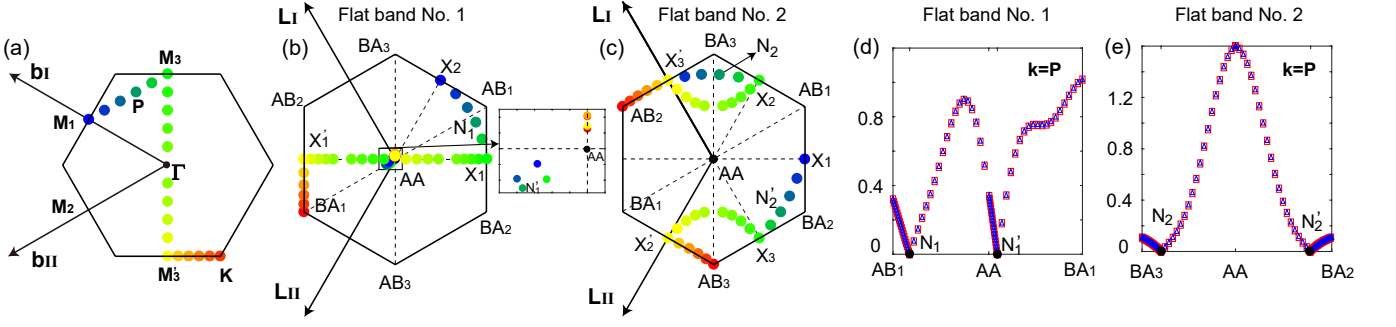


FIG. 4: (color online) (a) Momentum points at three paths M_1M_3 , M_3M_3' and $M_3'K$, which is denoted by circles in blue-green-yellow-red gradient color, and a general point $\mathbf{P} = 0.5\mathbf{b}_I - 0.3\mathbf{b}_{II}$. (b) and (c) Wave function nodal points for flat bands No. 1/2 in moiré unit cell indicated by corresponding colors in (a), and $N_1(N_1')$ and $N_2(N_2')$ are nodal points of flat bands No. 1/2 at $\mathbf{k} = \mathbf{P}$. (d) and (e) The norm of wave functions $\psi_{\mathbf{k},1/2}(\mathbf{r})$ for flat bands No.1/2 in moiré unit cell at $\mathbf{k} = \mathbf{P}$, and the wave functions from Hamiltonian $H^\varphi(\mathbf{r})$ and Eq.6/7 are labelled in red squares and blue triangles.

$\psi_{\mathbf{K}}(\mathbf{r})$ pinned at zero energy at \mathbf{K} , which is a good starting point to construct wave functions of the flat bands at other \mathbf{k} . As $\mathbf{k} \neq \mathbf{K}$, the conjectural wave function can be written as $\psi_{\mathbf{k}}(\mathbf{r}) \equiv f_{\mathbf{k}}(z)\psi_{\mathbf{K}}(\mathbf{r})$ with $z = x + iy$ since $D^\varphi(\mathbf{r})\psi_{\mathbf{k}}(\mathbf{k}) = f_{\mathbf{k}}(z)[D^\varphi(\mathbf{r})\psi_{\mathbf{K}}(\mathbf{r})] = 0$. The holomorphic function $f_{\mathbf{k}}(z)$ is either a constant or unbounded by Liouville's theorem, indicating that $f_{\mathbf{k}}(z)$ is meromorphic and thus has poles as $\mathbf{k} \neq \mathbf{K}$. The eigenfunctions $\psi_{\mathbf{k}}(\mathbf{r})$ are valid when the poles of $f_{\mathbf{k}}(z)$ are smoothed out by the nodes of $\psi_{\mathbf{K}}(\mathbf{r})$ in the Moiré unit cell. For the double flat bands in the conventional TBG, only one node appears in $\psi_{\mathbf{K}}(\mathbf{r})$. Differently, for the quadruple flat bands, a second-order node at AB stacking point emerges in $\psi_{\mathbf{K},2}(\mathbf{r})$ of the band No.2 at the magic α , while there are already two linear nodes in the $\psi_{\mathbf{K},1}(\mathbf{r})$ of the band No.1. We note that $\psi_{\mathbf{K},2}(\mathbf{r})$ is always pinned at the zero-energy and possesses the node only at the magic α . In contrast, $\psi_{\mathbf{K},1}(\mathbf{r})$ always has the two nodes and drops to zero energy at the magic α . The zero energy and the presence of the nodes at the magic α lead to the solution of the zero-energy absolutely flat bands in the entire Moiré BZ.

We turn to the detailed construction of wave functions for the quadruple flat bands. To cancel the poles of $\Psi_{\mathbf{K}}(\mathbf{r})$, we choose two theta functions in the denominator of $f_{\mathbf{k}}(z)$ and adjust $f_{\mathbf{k}}(z)$ to render the two-component wave function $\psi_{\mathbf{k}}(\mathbf{r})$ to obey the Bloch boundary conditions on moiré lattice vectors $\mathbf{L}_{I/II}$, namely $\psi_{\mathbf{k}}(\mathbf{r} + \mathbf{L}_{I/II}) = e^{i\mathbf{k} \cdot \mathbf{L}_{I/II}} U \psi_{\mathbf{k}}(\mathbf{r})$ with $U = \text{diag}(e^{-i\phi}, e^{i\phi})$ [23]. The analytical expressions for the quadruple-flat-band wave functions $\Psi_{\mathbf{k},1/2}(\mathbf{r})$ read,

$$\Psi_{\mathbf{k},1}(\mathbf{r}) = \frac{\vartheta_{a_1, b_1}(\nu|\omega)\vartheta_{a'_1, b'_1}(\nu|\omega)}{\vartheta_{\frac{1}{2}, \frac{1}{2}}(\nu|\omega)\vartheta_{\frac{5}{6}, \frac{7}{6}}(\nu|\omega)} \Psi_{\mathbf{K},1}(\mathbf{r}), \quad (6)$$

$$\Psi_{\mathbf{k},2}(\mathbf{r}) = \frac{\vartheta_{a_2, b_2}(\nu|\omega)\vartheta_{a'_2, b'_2}(\nu|\omega)}{[\vartheta_{\frac{7}{6}, \frac{5}{6}}(\nu|\omega)]^2} \Psi_{\mathbf{K},2}(\mathbf{r}), \quad (7)$$

with $\nu = z/L_I$, $\omega = \frac{L_{II}}{L_I} = e^{i\phi}$ and $L_{I/II} = (\mathbf{L}_{I/II})_x + i(\mathbf{L}_{I/II})_y$. To satisfy the Bloch boundary conditions, the rational charac-

teristics a and b obey

$$a_i + a'_i = \frac{1}{3} + \frac{(\mathbf{k} - \mathbf{K}) \cdot \mathbf{L}_I}{2\pi} + n_I, \quad (8)$$

$$b_i + b'_i = \frac{2}{3} - \frac{(\mathbf{k} - \mathbf{K}) \cdot \mathbf{L}_{II}}{2\pi} + n_{II}, \quad (9)$$

where n_I and n_{II} are arbitrary integers due to the lattice translational symmetry. The definition of the theta function $\vartheta_{a,b}(\nu|\omega)$ and the detailed derivations of Eq.6/7 are provided in the SM. The equations above cannot determine the explicit expressions of the rational characteristics, which are functions of \mathbf{k} , unless the node locations are given. The two nodal locations of $\psi_{\mathbf{k},i}(\mathbf{r})$ are denoted as $l_i\mathbf{L}_I + m_i\mathbf{L}_{II}$ and $l'_i\mathbf{L}_I + m'_i\mathbf{L}_{II}$ in the moiré unit cell, abbreviated as (l_i, m_i) and (l'_i, m'_i) . As $\vartheta_{a,b}(\nu|\omega)$ function's node is at $(\frac{1}{2} - b, \frac{1}{2} - a)$, we can get $l_i = \frac{1}{2} - b_i$ ($l'_i = \frac{1}{2} - b'_i$) and $m_i = \frac{1}{2} - a_i$ ($m'_i = \frac{1}{2} - a'_i$) from Eq.6/7. However, the node locations can be obtained only by numerical calculations. Instead of the explicit expressions of the wave functions, in the following, we will numerically confirm the validity of the expressions Eq.6/7 and the relation between Eq.8/9 and nodal coordinates.

As the momentum \mathbf{k} varies in the moiré BZ, the nodal points for the flat bands move in real space and their coordinates should obey Eq.8/9. We take three representative paths M_1M_3 , M_3M_3' (C_{2y} -symmetric) and $M_3'K$ (C_{2x} -symmetric) to show how nodal points evolve in the moiré unit cell, which is denoted by circles with blue-green-yellow-red gradient color in Fig.4(a). The corresponding evolution of nodes for bands No.1,2 in the moiré unit cell is displayed in Fig.4 (b) and (c). As previously discussed, the norm of wave functions $\psi_{\mathbf{k}}(\mathbf{r})$ on the C_{2y} -symmetric M_3M_3' path and C_{2x} -symmetric $M_3'K$ path preserves C_{2x}^r and C_{2y}^r symmetries in the real space, respectively. When \mathbf{k} is located at M_1 point, the flat band wave function $\psi_{\mathbf{k},1}$ ($\psi_{\mathbf{k},2}$) has two nodal points at AA (X_3') and X_2 (X_1). As \mathbf{k} varies from M_1 to M_3 , for $\psi_{\mathbf{k},1}$ one nodal point moves continuously from X_2 to X_1 , while the other first moves away from AA and then returns. Correspondingly, two nodal points of the $\psi_{\mathbf{k},2}$ move to X_2 and X_3 . It is apparent that the nodes of both bands are C_{2x}^r -symmetric at M_3 . With \mathbf{k} further varying along the C_{2y} -

symmetric $M_3M'_3$ path, both nodes of $\psi_{\mathbf{k},1}$ move along the X_1 -AA lines, and nodes of $\psi_{\mathbf{k},1}$ move from X_2/X_3 to X'_3/X'_2 , preserving C_{2x}^r symmetry. Finally, as \mathbf{k} varies along the the C_{2x} -symmetric $M'_3\mathbf{K}$ path, one nodal point of $\psi_{\mathbf{k},1}$ moves along X'_1 -BA₁ line and the other first moves away from AA along AA-BA₃ line and then returns. In contrast, both nodes of the $\psi_{\mathbf{k},2}$ move towards the AB stacking point and merge to form a second-order node at \mathbf{K} , consistent with our previous analysis. The evolution of nodal points along other high-symmetry paths is discussed in the SM. Moreover, we find that the coordinates of nodal points along the above paths numerically satisfies the Eq.8/9.

To prove the absolutely flat bands, we numerically calculate the flat-band wave functions from Hamiltonian $H^\varphi(\mathbf{r})$ and determine the node locations for several \mathbf{k} . The node locations fix the values of a , b in the theta function of Eq.6/7. To confirm the validity of the wave function expressions in Eq.6/7, we first select a general point \mathbf{P} in Fig.4(a) as an example. Fig.4 (d) and (e) show the norm of wave functions $\psi_{\mathbf{k},1/2}$ for flat band No.1/2 at a general point \mathbf{P} , where the wave functions from Hamiltonian $H^\varphi(\mathbf{r})$ and Eq.6/7 are labelled in red squares and blue triangles, respectively. We find a good agreement between them, and the agreement can be extended to other general \mathbf{k} points (see SM). Therefore, through the evolution of nodes and real-space wavefunction, we have verified the validity of wave function in Eq.6/7, and the quadruple flat

bands are absolutely flat.

Discussion—The alternative fluxes in the honeycomb lattice could be realized by a loop current state[27] or an antiferromagnetic a substrate. The multiple fold flat bands offer an ideal platform to explore the correlated quantum states. Besides the valley and sublattice degree of freedom in double flat bands[27], there is an emergent orbital degree of freedom in the quadruple flat bands, which will significantly enrich the correlated states. For example, an intervalley coherent state with an orbital polarization may be favored at proper interaction setting. In addition, high Chern numbers can realized in the quantum/valley Hall states at even integer filling and quantum anomalous Hall at odd integer filling[27–29]. With a fractional filling of the high-Chern-number flat bands[30], fractional quantum Hall states at a variety of filling factors can be realized.

Conclusion— In summary, we report that the double and quadruple absolutely flat bands appear recursively in TBG with alternative magnetic fluxes, and adjusting twisted angle and magnetic phase can control the transition between double and quadruple flat bands. The quadruple flat bands share the same origin with the conventional TBG, and by using holomorphic functions, we can generate analytical wave functions to explain the quadruple flat bands.

Acknowledgments— We thank Zhida Song and Simon Becker for the helpful discussions and comments.

-
- [1] R. Bistritzer and A. H. MacDonald, *Proc. Natl. Acad. Sci.* **108**, 12233 (2011).
- [2] Y. Cao, V. Fatemi, A. Demir, S. Fang, S. L. Tomarken, J. Y. Luo, J. D. Sanchez-Yamagishi, K. Watanabe, T. Taniguchi, E. Kaxiras, R. C. Ashoori, and P. Jarillo-Herrero, *Nature* **556**, 80 (2018).
- [3] Y. Cao, V. Fatemi, S. Fang, K. Watanabe, T. Taniguchi, E. Kaxiras, and P. Jarillo-Herrero, *Nature* **556**, 43 (2018).
- [4] H. C. Po, L. Zou, A. Vishwanath, and T. Senthil, *Phys. Rev. X* **8**, 031089 (2018).
- [5] X. Lu, P. Stepanov, W. Yang, M. Xie, M. A. Aamir, I. Das, C. Urgell, K. Watanabe, T. Taniguchi, G. Zhang, A. Bachtold, A. H. MacDonald, and D. K. Efetov, *Nature* **574**, 653 (2019).
- [6] G. Chen, L. Jiang, S. Wu, B. Lyu, H. Li, B. L. Chittari, K. Watanabe, T. Taniguchi, Z. Shi, J. Jung, et al., *Nature Physics* **15**, 237 (2019).
- [7] G. Chen, A. L. Sharpe, P. Gallagher, I. T. Rosen, E. J. Fox, L. Jiang, B. Lyu, H. Li, K. Watanabe, T. Taniguchi, et al., *Nature* **572**, 215 (2019).
- [8] T. Devakul, V. Crépel, Y. Zhang, and L. Fu, *Nature communications* **12**, 1 (2021).
- [9] A. Ghiotto, E.-M. Shih, G. S. Pereira, D. A. Rhodes, B. Kim, J. Zang, A. J. Millis, K. Watanabe, T. Taniguchi, J. C. Hone, et al., *Nature* **597**, 345 (2021).
- [10] P. J. Ledwith, A. Vishwanath, and E. Khalaf, *Phys. Rev. Lett.* **128**, 176404 (2022).
- [11] C. Zhang, T. Zhu, S. Kahn, S. Li, B. Yang, C. Herbig, X. Wu, H. Li, K. Watanabe, T. Taniguchi, et al., *Nature communications* **12**, 1 (2021).
- [12] L.-H. Tong, Q. Tong, L.-Z. Yang, Y.-Y. Zhou, Q. Wu, Y. Tian, L. Zhang, L. Zhang, Z. Qin, and L.-J. Yin, *Phys. Rev. Lett.* **128**, 126401 (2022).
- [13] C. Shen, Y. Chu, Q. Wu, N. Li, S. Wang, Y. Zhao, J. Tang, J. Liu, J. Tian, K. Watanabe, T. Taniguchi, R. Yang, Z. Y. Meng, D. Shi, O. V. Yazyev, and G. Zhang, *Nature Physics* **16**, 520 (2020).
- [14] U. Zondiner, A. Rozen, D. Rodan-Legrain, Y. Cao, R. Queiroz, T. Taniguchi, K. Watanabe, Y. Oreg, F. von Oppen, A. Stern, et al., *Nature* **582**, 203 (2020).
- [15] D. Wong, K. P. Nuckolls, M. Oh, B. Lian, Y. Xie, S. Jeon, K. Watanabe, T. Taniguchi, B. A. Bernevig, and A. Yazdani, *Nature* **582**, 198 (2020).
- [16] I. Das, C. Shen, A. Jaoui, J. Herzog-Arbeitman, A. Chew, C.-W. Cho, K. Watanabe, T. Taniguchi, B. A. Piot, B. A. Bernevig, and D. K. Efetov, *Phys. Rev. Lett.* **128**, 217701 (2022).
- [17] M. Christos, S. Sachdev, and M. S. Scheurer, *Physical Review X* **12**, 021018 (2022).
- [18] M. Yankowitz, S. Chen, H. Polshyn, Y. Zhang, K. Watanabe, T. Taniguchi, D. Graf, A. F. Young, and C. R. Dean, *Science* **363**, 1059 (2019).
- [19] P. Stepanov, I. Das, X. Lu, A. Fahimniya, K. Watanabe, T. Taniguchi, F. H. Koppens, J. Lischner, L. Levitov, and D. K. Efetov, *Nature* **583**, 375 (2020).
- [20] M. Serlin, C. L. Tschirhart, H. Polshyn, Y. Zhang, J. Zhu, K. Watanabe, T. Taniguchi, L. Balents, and A. F. Young, *Science* **367**, 900 (2020).
- [21] A. L. Sharpe, E. J. Fox, A. W. Barnard, J. Finney, K. Watanabe, T. Taniguchi, M. A. Kastner, and D. Goldhaber-Gordon, *Science* **365**, 605 (2019).
- [22] W.-Y. He, D. Goldhaber-Gordon, and K. T. Law, *Nature Communications* **11**, 1650 (2020).
- [23] G. Tarnopolsky, A. J. Kruchkov, and A. Vishwanath, *Physical review letters* **122**, 106405 (2019).

- [24] S. Becker, M. Embree, J. Wittsten, and M. Zworski, *Physical Review B* **103**, 165113 (2021).
- [25] S. Becker, M. Embree, J. Wittsten, and M. Zworski, *Probability and Mathematical Physics* **3**, 69 (2022).
- [26] F. D. M. Haldane, *Phys. Rev. Lett.* **61**, 2015 (1988).
- [27] N. Bultinck, E. Khalaf, S. Liu, S. Chatterjee, A. Vishwanath, and M. P. Zaletel, *Phys. Rev. X* **10**, 031034 (2020).
- [28] Y.-H. Zhang, D. Mao, Y. Cao, P. Jarillo-Herrero, and T. Senthil, *Phys. Rev. B* **99**, 075127 (2019).
- [29] Y.-H. Zhang, D. Mao, and T. Senthil, *Phys. Rev. Research* **1**, 033126 (2019).
- [30] P. J. Ledwith, G. Tarnopolsky, E. Khalaf, and A. Vishwanath, *Phys. Rev. Research* **2**, 023237 (2020).

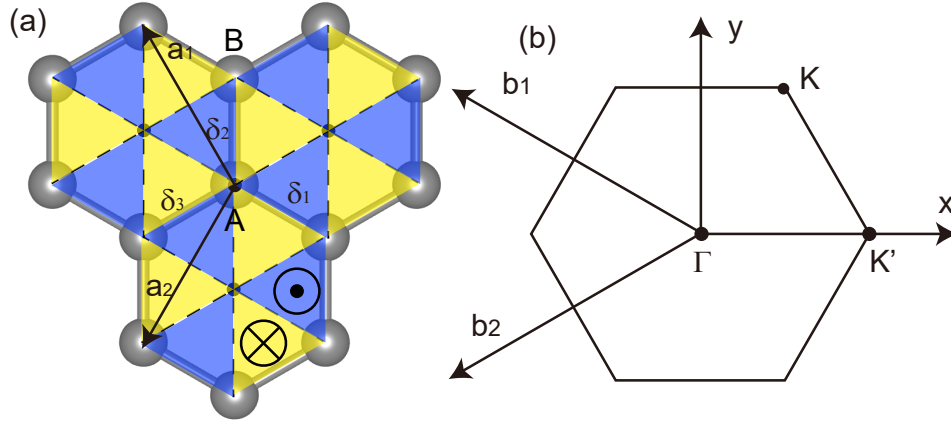


FIG. 5: (color online) (a) Distribution of periodic local magnetic fluxes in hexagonal plaquette of monolayer graphene with sublattices A and B. The blue region (\odot) and yellow region (\otimes) denote outward-to-the-plane and inward-to-the-plane magnetic fluxes, respectively. (b) The monolayer Brillouin Zone.

Appendix A: Continuum model of TBG and symmetry analysis

In this section, we give the derivation of chirally symmetric continuum model of TBG with magnetic phase, and discuss the symmetry of Hamiltonian $H^\varphi(\mathbf{r})$, also including approximate symmetries in the low energy and symmetry of wave function in the real space. In addition, we discuss relation of zero energy eigenstates between $D_{\mathbf{k}}^\varphi(\mathbf{r})$ and $T_{\mathbf{k}}$, and topological properties for the double and quadruple flat bands.

1. Chirally symmetric continuum model of TBG with magnetic phase and corresponding symmetry analysis

The monolayer graphene with sublattices A and B, shown in Fig.5(a), has the translation vectors $\mathbf{a}_1 = a(-\frac{1}{2}, \frac{\sqrt{3}}{2})$ and $\mathbf{a}_2 = a(-\frac{1}{2}, -\frac{\sqrt{3}}{2})$ with lattice constant a , and the corresponding reciprocal lattice vectors shown in Fig.5(b) are $\mathbf{b}_1 = \frac{4\pi}{a\sqrt{3}}(-\frac{\sqrt{3}}{2}, \frac{1}{2})$ and $\mathbf{b}_2 = \frac{4\pi}{a\sqrt{3}}(-\frac{\sqrt{3}}{2}, -\frac{1}{2})$. It is known that there are two Dirac points at \mathbf{K} and \mathbf{K}' points in monolayer graphene, which can be described by the p_z orbital including three nearest neighbor hoppings. Then, the tight binding Hamiltonian can be written as

$$H(\mathbf{k}) = \begin{pmatrix} 0 & h_{12}(\mathbf{k}) \\ h_{12}^*(\mathbf{k}) & 0 \end{pmatrix}, \quad (\text{A1})$$

where $h_{12}(\mathbf{k}) = t(e^{i\mathbf{k}\cdot\delta_1} + e^{i\mathbf{k}\cdot\delta_2} + e^{i\mathbf{k}\cdot\delta_3})$ with the nearest-neighbor hopping t along the δ bonds with $\delta_1 = a(\frac{1}{2}, -\frac{\sqrt{3}}{6})$, $\delta_2 = a(0, \frac{\sqrt{3}}{3})$ and $\delta_3 = a(-\frac{1}{2}, -\frac{\sqrt{3}}{6})$ bonds shown in Fig.5(a). Expanding Eq.A1 to first order around \mathbf{K} and under gauge transformation $g = \text{diag}(e^{-i\frac{\varphi}{3}}, e^{i\frac{\varphi}{3}})$, we can get the standard Dirac Hamiltonian $h_D(\mathbf{K} + \mathbf{k}) = -v_0(\sigma_x \mathbf{k}_x + \sigma_y \mathbf{k}_y)$ with Dirac velocity $v_0 = -\frac{\sqrt{3}}{2}t$.

We consider an periodic alternative magnetic fluxes in monolayer graphene, as shown in Fig.5(a), where the blue region (\odot) and yellow region (\otimes) denote outward-to-the-plane and inward-to-the-plane magnetic fluxes. The effect of the alternative magnetic fluxes is to multiply a phase φ for nearest-neighbor hopping, and then the tight binding Hamiltonian becomes

$$H^\varphi(\mathbf{k}) = \begin{pmatrix} 0 & e^{i\varphi} h_{12}(\mathbf{k}) \\ e^{-i\varphi} h_{12}^*(\mathbf{k}) & 0 \end{pmatrix}. \quad (\text{A2})$$

Then, the corresponding Dirac Hamiltonian around \mathbf{K} becomes

$$h_D^\varphi(\mathbf{K} + \mathbf{k}) = -v_0 \begin{pmatrix} 0 & e^{i\varphi}(\mathbf{k}_x - i\mathbf{k}_y) \\ e^{-i\varphi}(\mathbf{k}_x + i\mathbf{k}_y) & 0 \end{pmatrix}.$$

In the real space, the Hamiltonian $h_D^\varphi(\mathbf{K} + \mathbf{k})$ can be written as

$$h_D^\varphi(\mathbf{r}) = -v_0 \begin{pmatrix} 0 & e^{i\varphi}2\partial \\ e^{-i\varphi}2\bar{\partial} & 0 \end{pmatrix}, \quad (\text{A3})$$

where $\partial = \frac{1}{2i}(\partial_x - i\partial_y)$ and $\bar{\partial} = \frac{1}{2i}(\partial_x + i\partial_y)$. Hence, in the basis of $\Phi(\mathbf{r}) = (\psi_A^t, \chi_B^t, \psi_A^b, \chi_B^b)^T$ with layer index t/b , the chirally symmetric model of TBG with magnetic phase can be written as

$$H^\varphi(\mathbf{r}) = \begin{pmatrix} 0 & e^{i\varphi}2\partial & 0 & e^{i\beta}\alpha_0U^*(-\mathbf{r}) \\ e^{-i\varphi}2\bar{\partial} & 0 & e^{i\beta}\alpha_0U(\mathbf{r}) & 0 \\ 0 & e^{-i\beta}\alpha_0U^*(\mathbf{r}) & 0 & e^{i\varphi}2\partial \\ e^{-i\beta}\alpha_0U(-\mathbf{r}) & 0 & e^{-i\varphi}2\bar{\partial} & 0 \end{pmatrix}. \quad (\text{A4})$$

By reshuffling the basis to $\Phi(\mathbf{r}) = (\psi_A^t, \psi_A^b, \chi_B^t, \chi_B^b)^T$, the chirally symmetric continuum model reads

$$H^\varphi(\mathbf{r}) = \begin{pmatrix} 0 & 0 & e^{i\varphi}2\partial & e^{i\beta}\alpha_0U^*(-\mathbf{r}) \\ 0 & 0 & e^{-i\beta}\alpha_0U^*(\mathbf{r}) & e^{i\varphi}2\bar{\partial} \\ e^{-i\varphi}2\bar{\partial} & e^{i\beta}\alpha_0U(\mathbf{r}) & 0 & 0 \\ e^{-i\beta}\alpha_0U(-\mathbf{r}) & e^{-i\varphi}2\bar{\partial} & 0 & 0 \end{pmatrix}. \quad (\text{A5})$$

After gauge transformation $g_\varphi = \text{diag}(e^{i\frac{\varphi}{2}}, e^{i\frac{\varphi}{2}}, e^{-i\frac{\varphi}{2}}, e^{-i\frac{\varphi}{2}})$, the Hamiltonian $H^\varphi(\mathbf{r})$ becomes

$$H^\varphi(\mathbf{r}) = \begin{pmatrix} 0 & 0 & 2\partial & e^{i(-\varphi+\beta)}\alpha_0U^*(-\mathbf{r}) \\ 0 & 0 & e^{i(-\varphi-\beta)}\alpha_0U^*(\mathbf{r}) & 2\bar{\partial} \\ 2\bar{\partial} & e^{i(\varphi+\beta)}\alpha_0U(\mathbf{r}) & 0 & 0 \\ e^{i(\varphi-\beta)}\alpha_0U(-\mathbf{r}) & 2\bar{\partial} & 0 & 0 \end{pmatrix}. \quad (\text{A6})$$

Under gauge transformation $g_\beta = \text{diag}(e^{-i\frac{\beta}{2}}, e^{i\frac{\beta}{2}}, e^{-i\frac{\beta}{2}}, e^{i\frac{\beta}{2}})$, the global phase β can be gauged away, and then the Hamiltonian $H^\varphi(\mathbf{r})$ becomes

$$H^\varphi(\mathbf{r}) = \begin{pmatrix} 0 & D^{\varphi*}(-\mathbf{r}) \\ D^\varphi(\mathbf{r}) & 0 \end{pmatrix}, D^\varphi(\mathbf{r}) = \begin{pmatrix} 2\bar{\partial} & \alpha(\varphi)U(\mathbf{r}) \\ \alpha(\varphi)U(-\mathbf{r}) & 2\bar{\partial} \end{pmatrix}, \quad (\text{A7})$$

where we define a complex parameter $\alpha(\varphi) = \alpha_0 e^{i\varphi}$. The chiral symmetric model $H(\mathbf{r})$ ($\varphi = 0$) of conventional TBG without alternative fluxes can be written as

$$H(\mathbf{r}) = \begin{pmatrix} 0 & D^*(-\mathbf{r}) \\ D(\mathbf{r}) & 0 \end{pmatrix}, D(\mathbf{r}) = \begin{pmatrix} 2\bar{\partial} & \alpha_0U(\mathbf{r}) \\ \alpha_0U(-\mathbf{r}) & 2\bar{\partial} \end{pmatrix},$$

which has magnetic point group $6'22'$, including $C_{3z} = e^{i\frac{2\pi}{3}\tau_z}\sigma_0$, $C_{2z}T = \tau_x\sigma_0\mathcal{K}$, $C_{2y} = \tau_y\sigma_y$ and $C_{2x}T = i\tau_z\sigma_y\mathcal{K}$, where T is time reversal operator and \mathcal{K} is the complex conjugation. These symmetries and the moiré translations generate the magnetic space group $P6'2'2$ (No.177.151 in BNS settings). In addition, we can define an anti-unitary particle-hole operator $\mathcal{P} = i\tau_x\sigma_y\mathcal{K}$, which satisfies $\mathcal{P}^2 = -1$. It acts on the chiral symmetric continuum model $H(\mathbf{r})$ as

$$\mathcal{P}H(\mathbf{r})\mathcal{P}^{-1} = -H(\mathbf{r}). \quad (\text{A8})$$

A chiral operator also can be defined $S = \tau_z\sigma_0$ with $S^2 = 1$. Under chiral symmetry S , the chiral symmetric continuum model $H(\mathbf{r})$ transforms as

$$SH(\mathbf{r})S^{-1} = -H(\mathbf{r}). \quad (\text{A9})$$

Combined particle-hole and chiral operators, we can define an effective time reversal operator $\tilde{T} = \tau_y\sigma_y\mathcal{K}$ with $\tilde{T}^2 = 1$, and then the model $H(\mathbf{r})$ transforms as

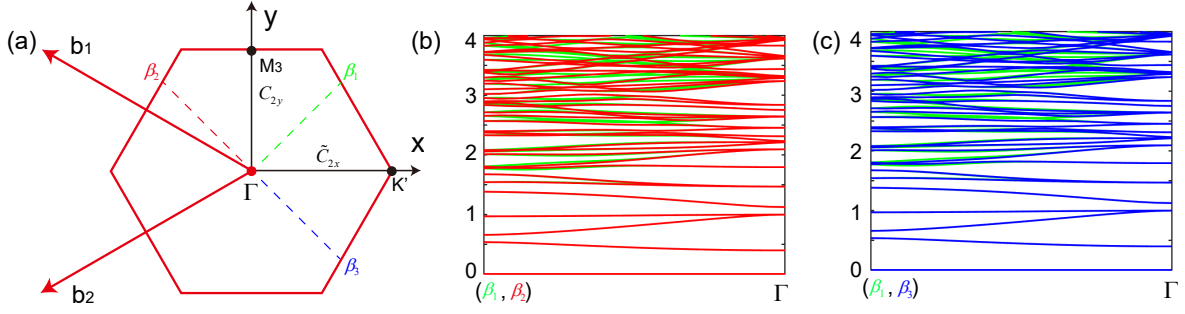


FIG. 6: (color online) (a) Three general lines $\Gamma\beta_1$, $\Gamma\beta_2$ and $\Gamma\beta_3$ in moiré BZ are connected each other by C_{2x} and C_{2y} symmetries. (b) The band structure along $\Gamma\beta_1$ and $\Gamma\beta_2$. (c) The band structure along $\Gamma\beta_1$ and $\Gamma\beta_3$. The green, red and blue label the band structure along $\Gamma\beta_1$, $\Gamma\beta_2$ and $\Gamma\beta_3$, respectively.

$$\tilde{T}H(\mathbf{r})\tilde{T}^{-1} = H(\mathbf{r}). \quad (\text{A10})$$

Due to effective time reversal operator \tilde{T} , we can also define another crystalline symmetries, including $C_{2z} = i\tau_z\sigma_y$ and $C_{2x} = \tau_x\sigma_0$.

After considering alternative magnetic fluxes, C_{2x} and C_{2y} are broken due to phase $e^{i\varphi}$, the magnetic point group becomes $P6'$ (No.168.111 in BNS settings) with magnetic point group $6'$, including $C_{3z} = e^{i\frac{2\pi}{3}\tau_z}\sigma_0$ and $C_{2z}T = \tau_x\sigma_0\mathcal{K}$. Particle-hole operator $\mathcal{P} = i\tau_x\sigma_y\mathcal{K}$, chiral operator $S = \tau_z\sigma_0$ and effective time reversal operator $\tilde{T} = \tau_y\sigma_y\mathcal{K}$ are always preserved.

2. Approximate symmetries in the low energy

In the low energy, the Hamiltonian $H^\varphi(\mathbf{r})$ has approximate rotational symmetries $C_{2x} = \tau_x\sigma_0$ and $C_{2y} = \tau_y\sigma_y$, where the gauge in symmetry are chosen to keep the interlayer coupling invariant and change monolayer Dirac Hamiltonian. We can define the Hamiltonian difference $\Delta H_{x/y}$ as

$$\Delta H_x = (C_{2x})H^\varphi(\mathbf{r})(C_{2x})^{-1} - H^\varphi(C_{2x}\mathbf{r}), \Delta H_y = (C_{2y})H^\varphi(\mathbf{r})(C_{2y})^{-1} - H^\varphi(C_{2y}\mathbf{r}). \quad (\text{A11})$$

Put $C_{2x} = \tau_x\sigma_0$ and $C_{2y} = \tau_y\sigma_y$ into Eq.A11, and then the Hamiltonian difference $\Delta H_{x/y}$ becomes

$$\Delta H_x = 2 \sin \varphi \begin{pmatrix} 0 & 0 & \partial & 0 \\ 0 & 0 & 0 & \partial \\ -\bar{\partial} & 0 & 0 & 0 \\ 0 & -\bar{\partial} & 0 & 0 \end{pmatrix}, \Delta H_y = -2 \sin \varphi \begin{pmatrix} 0 & 0 & \partial & 0 \\ 0 & 0 & 0 & \partial \\ -\bar{\partial} & 0 & 0 & 0 \\ 0 & -\bar{\partial} & 0 & 0 \end{pmatrix}, \quad (\text{A12})$$

here, $\varphi \neq \frac{\pi}{2}$. When $\varphi = \frac{\pi}{2}$, the Dirac Hamiltonian for monolayer is from $H_{Dirac} = -v\mathbf{k} \cdot \sigma$ to $H_{Dirac} = -v\mathbf{k} \times \sigma$, and the system with alternative magnetic field has exact rotational symmetries C_{2x} and C_{2y} .

In the momentum lattice, we can arrange the basis as $\hat{\Psi}_{\mathbf{k}} = \sum_{m,n} \oplus (\hat{\psi}_{A;\mathbf{k}+\mathbf{g}_{mn}}^t, \hat{\psi}_{B;\mathbf{k}+\mathbf{g}_{mn}}^t, \hat{\psi}_{A;\mathbf{k}+\mathbf{g}_{mn}+\mathbf{q}_1}^b, \hat{\psi}_{B;\mathbf{k}+\mathbf{g}_{mn}+\mathbf{q}_1}^b)^T$ with \mathbf{g}_{mn} being the lattice of momenta. Then, the the Hamiltonian difference $\Delta H_{x/y}$ can be rewritten as

$$\Delta H_{x/y} = \pm 2 \sin \varphi \sum_{m,n} \oplus \begin{pmatrix} (\mathbf{k}_x + \mathbf{g}_{mn,x})\sigma_x + (\mathbf{k}_y + \mathbf{g}_{mn,y})\sigma_y & 0 \\ 0 & (\mathbf{k}_x + \mathbf{g}_{mn,x} + \mathbf{q}_{1,x})\sigma_x + (\mathbf{k}_y + \mathbf{g}_{mn,y} + \mathbf{q}_{1,y})\sigma_y \end{pmatrix} \quad (\text{A13})$$

Hence, the Hamiltonian difference $\Delta H_{x/y}$ is proportional to the magnitude of momentum k . In the low energy, the momentum k is very small, and then ΔH approximately equal to zero, indicating that the low energy spectrum has C_{2x} and C_{2y} symmetries. Fig.6 (b) and (c) shows band structure with magnetic phase $\varphi = 0.254\pi$ at magic $\alpha_M = 1.379$ along general lines $\Gamma\beta_1$, $\Gamma\beta_2$ and $\Gamma\beta_3$ marked by green, red and blue, where $\Gamma\beta_{1,2,3}$ are connected each other by C_{2x} and C_{2y} symmetries. The general lines $\Gamma\beta_{1,2,3}$ are the same in the low energy, while the high energy spectrums are different, indicating that the low energy structure has C_{2x} and C_{2y} symmetries.

3. Symmetry of wave function $\Psi_{\mathbf{k}}(\mathbf{r})$ in the real space

By acting $C_{2z}T$ symmetry on four component wave function $\Psi_{\mathbf{k}}(\mathbf{r}) = (\psi_{\mathbf{k}}^\top(\mathbf{r}) \chi_{\mathbf{k}}^\top(\mathbf{r}))^\top$,

$$C_{2z}T \begin{pmatrix} \psi_{\mathbf{k}}(\mathbf{r}) \\ \chi_{\mathbf{k}}(\mathbf{r}) \end{pmatrix} = \begin{pmatrix} \chi_{\mathbf{k}}^*(\mathbf{r}) \\ \psi_{\mathbf{k}}^*(\mathbf{r}) \end{pmatrix} = \begin{pmatrix} \psi_{\mathbf{k}}(-\mathbf{r}) \\ \chi_{\mathbf{k}}(-\mathbf{r}) \end{pmatrix}, \quad (\text{A14})$$

Hence, $\chi_{\mathbf{k}}(\mathbf{r}) = \psi_{\mathbf{k}}^*(-\mathbf{r})$, and then we can get wave function $\Psi_{\mathbf{k}}(\mathbf{r}) = (\psi_{\mathbf{k}}^\top(\mathbf{r}) \psi_{\mathbf{k}}^\dagger(-\mathbf{r}))^\top$. Due to C_{2x} symmetry, the wave function $\Psi_{\mathbf{k}}(\mathbf{r})$ becomes

$$C_{2x} \begin{pmatrix} \psi_{\mathbf{k}}(\mathbf{r}) \\ \psi_{\mathbf{k}}^*(-\mathbf{r}) \end{pmatrix} = \begin{pmatrix} \psi_{\mathbf{k}}^*(-\mathbf{r}) \\ \psi_{\mathbf{k}}(\mathbf{r}) \end{pmatrix} = \begin{pmatrix} \psi_{C_{2x}\mathbf{k}}(C_{2x}\mathbf{r}) \\ \psi_{C_{2x}\mathbf{k}}^*(-C_{2x}\mathbf{r}) \end{pmatrix}. \quad (\text{A15})$$

Then, $\psi_{\mathbf{k}}(\mathbf{r}) = \psi_{C_{2x}\mathbf{k}}^*(-C_{2x}\mathbf{r})$. Hence, the norm of wave function $\psi_{\mathbf{k}}(\mathbf{r})$ on C_{2x} -symmetric \mathbf{k} path has C_{2y}^r symmetry in the real space. Similarly, the norm of wave function $\psi_{\mathbf{k}}(\mathbf{r})$ on C_{2y} -symmetric \mathbf{k} path has C_{2x}^r symmetry in the real space.

4. Relation of zero energy eigenstates between $D_{\mathbf{k}}^\varphi(\mathbf{r})$ and $T_{\mathbf{k}}$

The eigenfunction of Hamiltonian $H_{\mathbf{k}}^\varphi(\mathbf{r})$ can be written as

$$\begin{pmatrix} 0 & D_{\mathbf{k}}^{\varphi*}(-\mathbf{r}) \\ D_{\mathbf{k}}^\varphi(\mathbf{r}) & 0 \end{pmatrix} \begin{pmatrix} \psi_{\mathbf{k}}^n(\mathbf{r}) \\ \chi_{\mathbf{k}}^n(\mathbf{r}) \end{pmatrix} = E_{\mathbf{k}} \begin{pmatrix} \psi_{\mathbf{k}}^n(\mathbf{r}) \\ \chi_{\mathbf{k}}^n(\mathbf{r}) \end{pmatrix}, \quad (\text{A16})$$

where $\psi_{\mathbf{k}}^n(\mathbf{r})$ and $\chi_{\mathbf{k}}^n(\mathbf{r})$ are two component wave functions with n -fold degeneracy. For zero energy $E_{\mathbf{k}} = 0$, the eigenfunction becomes

$$D_{\mathbf{k}}^\varphi(\mathbf{r})\psi_{\mathbf{k}}^n(\mathbf{r}) = 0, \quad D_{\mathbf{k}}^{\varphi*}(-\mathbf{r})\chi_{\mathbf{k}}^n(\mathbf{r}) = 0. \quad (\text{A17})$$

Then, the eigenstates of $2n$ -fold degenerate flat bands with zero energy can be written as

$$\Psi_{\mathbf{k},1}^n(\mathbf{r}) = \begin{pmatrix} \psi_{\mathbf{k}}^n(\mathbf{r}) \\ 0 \end{pmatrix}, \quad \Psi_{\mathbf{k},2}^n(\mathbf{r}) = \begin{pmatrix} 0 \\ \chi_{\mathbf{k}}^n(\mathbf{r}) \end{pmatrix}, \quad (\text{A18})$$

Due to $\chi_{\mathbf{k}}(\mathbf{r}) = \psi_{\mathbf{k}}^*(-\mathbf{r})$, we can get

$$\Psi_{\mathbf{k},1}^n(\mathbf{r}) = \begin{pmatrix} \psi_{\mathbf{k}}^n(\mathbf{r}) \\ 0 \end{pmatrix}, \quad \Psi_{\mathbf{k},2}^n(\mathbf{r}) = \begin{pmatrix} 0 \\ \psi_{\mathbf{k}}^{*n}(-\mathbf{r}) \end{pmatrix}, \quad (\text{A19})$$

The relation between $D_{\mathbf{k}}^\varphi(\mathbf{r})$ and $T_{\mathbf{k}}$ reads

$$D_{\mathbf{k}}^\varphi(\mathbf{r}) = (2\bar{\partial} - \mathbf{k})(I - \alpha(\varphi)T_{\mathbf{k}}). \quad (\text{A20})$$

If $T_{\mathbf{k}}$ has eigenvalue $\frac{1}{\alpha(\varphi)}$ independent of \mathbf{k} , the eigenfunction reads

$$T_{\mathbf{k}}\phi_{\mathbf{k}}^n(\mathbf{r}) = \frac{1}{\alpha(\varphi)}\phi_{\mathbf{k}}^n(\mathbf{r}), \quad (\text{A21})$$

where $\phi_{\mathbf{k}}^n(\mathbf{r})$ are eigenvectors of $T_{\mathbf{k}}$ with n -fold degeneracy. Then, the eigenfunction of $D_{\mathbf{k}}^\varphi(\mathbf{r})$ can be written as

$$D_{\mathbf{k}}^\varphi(\mathbf{r})\phi_{\mathbf{k}}^n(\mathbf{r}) = (2\bar{\partial} - \mathbf{k})(I - \alpha(\varphi)T_{\mathbf{k}})\phi_{\mathbf{k}}^n(\mathbf{r}) = 0, \quad (\text{A22})$$

indicating that $\psi_{\mathbf{k}}^n(\mathbf{r}) = \phi_{\mathbf{k}}^n(\mathbf{r})$ are eigenvectors of $D_{\mathbf{k}}^\varphi(\mathbf{r})$ with n -fold degeneracy. Hence, based on Eq. A19, the non-degenerate and two-fold degenerate eigenvalues in the $T_{\mathbf{k}}$ spectrum correspond to zero energy double and quadruple flat bands.

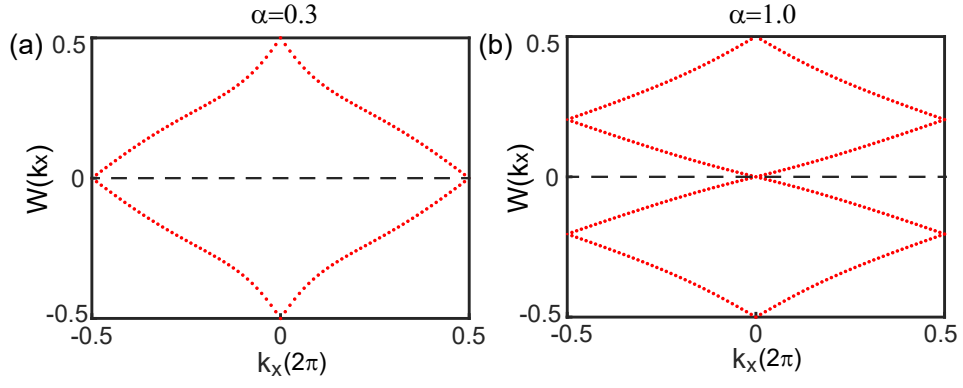


FIG. 7: (color online) The Wilson loops $W(\mathbf{k}_x)$ of the gapped bands in the TBG with magnetic field at (a) $\alpha = 0.3$ and (b) $\alpha = 1.0$. Momentum \mathbf{k}_x is along \mathbf{b}_1 direction.

5. Topological properties

We further explore the topological properties for the double and quadruple flat bands by calculating Wilson loops. According to Ref.[1], the topological invariant for the $2m$ middle bands gapped from high-energy and low-energy bands is \mathbb{Z}_2 protected by the \mathcal{P} symmetry. Fig.7(a) and (b) show the corresponding Wilson loops with corresponding $\alpha = 0.3$ and 1.0 , where we integrate along \mathbf{b}_{II} and plot the spectra along \mathbf{b}_I . In both cases, the partner switch in the Wannier centers from $\mathbf{k} = -\mathbf{b}_I/2$ to $\mathbf{k} = 0$, similar to topological insulators, indicates a nontrivial topology $\mathbb{Z}_2 = 1$. Moreover, by introducing a staggered potential on both layers, the quadruple (double) flat bands will split into two double (single) quasi-flat bands with ± 2 (± 1) Chern number.

Appendix B: Theta function and flat band Wave function

Here, the definitions and properties of theta function will be discussed, and then we give the derivation of analytical expressions for the quadruple-flat-band wave functions and the evolution of nodes in real space.

1. Theta function

The theta function can be defined as

$$\vartheta(z; \tau) = \sum_{n=-\infty}^{\infty} e^{\pi i \tau n^2 + 2\pi i n z} \quad (\text{B1})$$

Where $n \in \mathbb{Z}$, τ are complex parameters with $\text{Im}(\tau) > 0$, and z is complex variable. It can be checked that

$$\vartheta(z + 1|\tau) = \sum_{n=-\infty}^{+\infty} e^{\pi i \tau n^2 + 2\pi i n(z+1)} = \sum_{n=-\infty}^{+\infty} e^{\pi i \tau n^2 + 2\pi i n z} = \vartheta(z|\tau), \quad (\text{B2})$$

$$\vartheta(z + \tau|\tau) = \sum_{n=-\infty}^{+\infty} e^{\pi i \tau n^2 + 2\pi i n(z+\tau)} = e^{-\pi i \tau - 2\pi i z} \sum_{n=-\infty}^{+\infty} e^{\pi i (n+1)^2 \tau + 2\pi i (n+1)z} = e^{-\pi i \tau - 2\pi i z} \vartheta(z|\tau), \quad (\text{B3})$$

$$\vartheta(-z; \tau) = \sum_{n=-\infty}^{\infty} e^{\pi i \tau n^2 - 2\pi i n z} = \sum_{n=-\infty}^{\infty} e^{\pi i \tau (-n)^2 + 2\pi i (-n)z} = \vartheta(z; \tau) \quad (\text{B4})$$

All zeros of the theta functions are simple zeros and are given as

$$\vartheta(z, \tau) = 0 \iff z = m + n\tau + \frac{1}{2} + \frac{\tau}{2}. \quad (\text{B5})$$

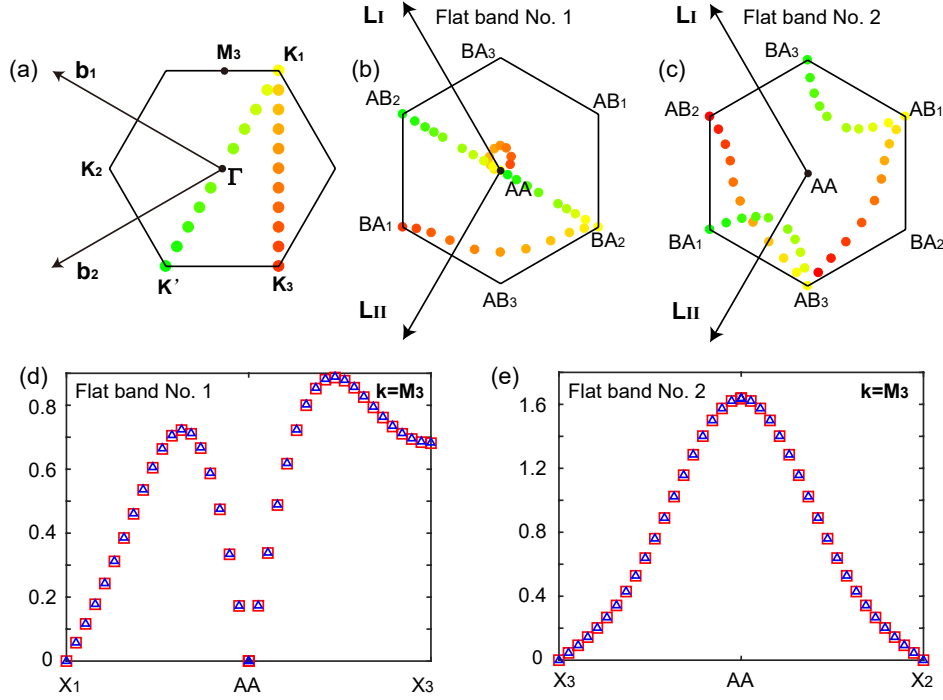


FIG. 8: (color online) (a) Momentum points at $\mathbf{K}'\mathbf{K}_1$ and $\mathbf{K}_1\mathbf{K}_3$ paths, which is denoted by circles with green-yellow-red gradient color, and a high point $\mathbf{M}_3 = 0.5\mathbf{b}_1 - 0.5\mathbf{b}_2$. (b) and (c) Wave function nodal points for flat bands No. 1/2 in moiré unit cell have corresponding colors in (a). (d) and (e) The absolute value of wave functions $|\Psi_{\mathbf{k},1/2}(\mathbf{r})|$ for flat bands No.1/2 in moiré unit cell at $\mathbf{k} = \mathbf{M}_3$, and the wave functions from Hamiltonian $H^\varphi(\mathbf{r})$ and Eq.B19/B23 are labelled in red squares and blue triangles.

The theta functions with rational characteristics a and b are defined as

$$\vartheta_{a,b}(z|\tau) = \sum_{n=-\infty}^{+\infty} e^{i\pi\tau(n+a)^2} e^{2i\pi(n+a)(z+b)}, \quad (\text{B6})$$

where τ are complex parameters with $\text{Im}(\tau) > 0$, and the range of a is $[0,1]$. z is complex variables. The relation between $\vartheta_{a,b}(z|\tau)$ and $\vartheta(z|\tau)$ is

$$\vartheta_{a,b}(z|\tau) = e^{\pi ia^2\tau + 2\pi ia(z+b)} \vartheta(z + a\tau + b, \tau). \quad (\text{B7})$$

Then, it can be checked that

$$\vartheta_{a,b}(z+1|\tau) = e^{2i\pi a} \vartheta_{a,b}(z|\tau), \vartheta_{a\pm 1,b}(z|\tau) = \vartheta_{a,b}(z|\tau), \vartheta_{a,b}(z+\tau|\tau) = e^{-2i\pi(z+b+\frac{\tau}{2})} \vartheta_{a,b}(z|\tau)m, \quad (\text{B8})$$

The simple zeros are

$$\vartheta_{a,b}(z|\tau) = 0 \leftrightarrow z = \frac{1+\tau}{2} - (a\tau + b) + (m\tau + n), m, n \in \mathbb{Z}, \quad (\text{B9})$$

2. Wave function for flat bands #1/2

In main text, we have discussed the nodal features of wave function at \mathbf{K} for flat bands No.1/2. For flat bands No.1, two nodes appear at the AA and BA stacking with linear real-space dependence. However, for flat band No.2, there is only one node at the AB stacking and the norm exhibits real-space quadratic dependence. Based on these nodal features, the analytical expressions for the quadruple-flat-band wave functions can be constructed as

$$\Psi_{\mathbf{k},i}(\mathbf{r}) = f_{\mathbf{k}}(z)\Psi_{\mathbf{K},i}(\mathbf{r}), f_{\mathbf{k}}(z) = \frac{\vartheta_{a,b}(\frac{z}{L_1}|\frac{L_2}{L_1})\vartheta_{a',b'}(\frac{z}{L_1}|\frac{L_2}{L_1})}{\vartheta_{e,f}(\frac{z}{L_1}|\frac{L_2}{L_1})\vartheta_{e',f'}(\frac{z}{L_1}|\frac{L_2}{L_1})}, \quad (\text{B10})$$

where $i = 1, 2$ is band index, and the origin of \mathbf{k} is chosen at Γ in the moiré BZ. a/a' and b/b' are functions of \mathbf{k} , while e/e' and f/f' are determined by nodal points of wave function $\Psi_{\mathbf{K},i}(\mathbf{r})$. The two nodal positions of $\Psi_{\mathbf{K},i}(\mathbf{r})$ are located at $c_{\text{I}}\mathbf{L}_{\text{I}} + c_{\text{II}}\mathbf{L}_{\text{II}}$ and $c'_{\text{I}}\mathbf{L}_{\text{I}} + c'_{\text{II}}\mathbf{L}_{\text{II}}$ in the moiré unit cell, which should coincide with the nodal points of $\vartheta_{e,f}(\frac{z}{L_1}|\frac{L_2}{L_1})$ and $\vartheta_{e',f'}(\frac{z}{L_1}|\frac{L_2}{L_1})$. Then, by using Eq.B9, we can get

$$e = \frac{1}{2} - c_{\text{II}}, f = \frac{1}{2} - c_{\text{I}}, e' = \frac{1}{2} - c'_{\text{II}}, f' = \frac{1}{2} - c'_{\text{I}} \quad (\text{B11})$$

According to Bloch theorem, due to $H_{\mathbf{k}}^{\varphi}(\mathbf{r} + \mathbf{L}_{\text{I/II}}) = UH_{\mathbf{k}}^{\varphi}(\mathbf{r})U^{-1}$ with $U = \text{diag}(e^{-i2\pi/3}, e^{i2\pi/3})$, the two component wave function $\Psi_{\mathbf{k},i}(\mathbf{r})$ shall obey the Bloch boundary condition

$$\Psi_{\mathbf{k},i}(\mathbf{r} + \mathbf{L}_{\text{I/II}}) = e^{i\mathbf{k}\cdot\mathbf{L}_{\text{I/II}}}U\Psi_{\mathbf{k},i}(\mathbf{r}). \quad (\text{B12})$$

Putting Eq.B10 into Eq.B12, $f_{\mathbf{k}}(z)$ also satisfies Bloch boundary condition

$$f_{\mathbf{k}}(z + \mathbf{L}_{\text{I/II}}) = e^{i(\mathbf{k}-\mathbf{K})\cdot\mathbf{L}_{\text{I/II}}}f_{\mathbf{k}}(z), \quad (\text{B13})$$

Then, by using $\vartheta_{a,b}(z + 1|\tau) = e^{2i\pi a}\vartheta_{a,b}(z|\tau)$ and $\vartheta_{a,b}(z + \tau|\tau) = e^{-2i\pi(z+b+\frac{\tau}{2})}$ in the Eq.B8, we can get

$$e^{2i\pi(a+a'-e-e')} = e^{i(\mathbf{k}-\mathbf{K})\cdot\mathbf{L}_{\text{I}}}, \quad e^{-2i\pi(b+b'-f-f')} = e^{i(\mathbf{k}-\mathbf{K})\cdot\mathbf{L}_{\text{II}}} \quad (\text{B14})$$

Therefore,

$$a + a' = e + e' + \frac{(\mathbf{k} - \mathbf{K}) \cdot \mathbf{L}_{\text{I}}}{2\pi}, \quad b + b' = f + f' - \frac{(\mathbf{k} - \mathbf{K}) \cdot \mathbf{L}_{\text{II}}}{2\pi}, \quad (\text{B15})$$

When the two nodal positions of $\Psi_{\mathbf{k},i}(\mathbf{r})$ are denoted as $l\mathbf{L}_{\text{I}} + m\mathbf{L}_{\text{II}}$ and $l'\mathbf{L}_{\text{I}} + m'\mathbf{L}_{\text{II}}$ in the moiré unit cell, abbreviated as (l,m) and (l',m') . From the Eq.B10, the two nodal positions are determined by $\vartheta_{a,b}(\frac{z}{L_1}|\frac{L_2}{L_1})$ and $\vartheta_{a',b'}(\frac{z}{L_1}|\frac{L_2}{L_1})$. Then, the relation between nodal coordinates and rational characteristics reads

$$l = \frac{1}{2} - b, l' = \frac{1}{2} - b', m = \frac{1}{2} - a, m' = \frac{1}{2} - a' \quad (\text{B16})$$

Combined with Eq.B15, the relation between nodal coordinates reads

$$m + m' = 1 - e - e' - \frac{(\mathbf{k} - \mathbf{K}) \cdot \mathbf{L}_{\text{I}}}{2\pi}, \quad l + l' = 1 - f - f' + \frac{(\mathbf{k} - \mathbf{K}) \cdot \mathbf{L}_{\text{II}}}{2\pi}, \quad (\text{B17})$$

For absolutely flat bands #1, the two nodal positions of $\Psi_{\mathbf{K},1}(\mathbf{r})$ are located at AA and BA stacking points with $\mathbf{r}_{AA} = 0$ and $\mathbf{r}_{BA} = \frac{-2\mathbf{L}_{\text{I}}-\mathbf{L}_{\text{II}}}{3}$, and we can get

$$e = \frac{1}{2}, \quad f = \frac{1}{2}, \quad e' = \frac{5}{6}, \quad f' = \frac{7}{6} \quad (\text{B18})$$

Hence, the wave function $\Psi_{\mathbf{k},1}(\mathbf{r})$ of flat bands #1 and relation between nodal coordinates and rational characteristics are

$$\Psi_{\mathbf{k},1}(\mathbf{r}) = \frac{\vartheta_{a_1,b_1}(\frac{z}{L_1}|\frac{L_2}{L_1})\vartheta_{a'_1,b'_1}(\frac{z}{L_1}|\frac{L_2}{L_1})}{\vartheta_{\frac{1}{2},\frac{1}{2}}(\frac{z}{L_1}|\frac{L_2}{L_1})\vartheta_{\frac{5}{6},\frac{7}{6}}(\frac{z}{L_1}|\frac{L_2}{L_1})}\Psi_{\mathbf{K},1}(\mathbf{r}), \quad (\text{B19})$$

$$a_1 + a'_1 = \frac{4}{3} + \frac{(\mathbf{k} - \mathbf{K}) \cdot \mathbf{L}_I}{2\pi}, \quad b_1 + b'_1 = \frac{5}{3} - \frac{(\mathbf{k} - \mathbf{K}) \cdot \mathbf{L}_{II}}{2\pi}, \quad (\text{B20})$$

The corresponding relation between nodal coordinates is

$$l_1 + l'_1 = -\frac{2}{3} + \frac{(\mathbf{k} - \mathbf{K}) \cdot \mathbf{L}_{II}}{2\pi}, \quad m_1 + m'_1 = -\frac{1}{3} - \frac{(\mathbf{k} - \mathbf{K}) \cdot \mathbf{L}_I}{2\pi}. \quad (\text{B21})$$

For flat bands #2, the nodal point of $\psi_{\mathbf{K},2}(\mathbf{r})$ is located at AB stacking point with $\mathbf{r}_{AB} = \frac{-\mathbf{L}_I + \mathbf{L}_{II}}{3}$

$$e = \frac{1}{6}, \quad f = \frac{5}{6}, \quad e' = \frac{1}{6}, \quad f' = \frac{5}{6} \quad (\text{B22})$$

Hence, the wave function $\Psi_{\mathbf{k},2}(\mathbf{r})$ of flat bands #2 and relation between nodal coordinates and rational characteristics are

$$\Psi_{\mathbf{k},2}(\mathbf{r}) = \frac{\vartheta_{a_2, b_2}(\frac{z}{L_1} | \frac{L_2}{L_1}) \vartheta_{a'_2, b'_2}(\frac{z}{L_1} | \frac{L_2}{L_1})}{[\vartheta_{\frac{1}{6}, \frac{5}{6}}(\frac{z}{L_1} | \frac{L_2}{L_1})]^2} \Psi_{\mathbf{K},2}(\mathbf{r}), \quad (\text{B23})$$

$$a_2 + a'_2 = \frac{1}{3} + \frac{(\mathbf{k} - \mathbf{K}) \cdot \mathbf{L}_I}{2\pi}, \quad b_2 + b'_2 = \frac{5}{3} - \frac{(\mathbf{k} - \mathbf{K}) \cdot \mathbf{L}_{II}}{2\pi}, \quad (\text{B24})$$

The corresponding relation between nodal coordinates is

$$l_2 + l'_2 = -\frac{2}{3} + \frac{(\mathbf{k} - \mathbf{K}) \cdot \mathbf{L}_{II}}{2\pi}, \quad m_2 + m'_2 = \frac{2}{3} - \frac{(\mathbf{k} - \mathbf{K}) \cdot \mathbf{L}_I}{2\pi}. \quad (\text{B25})$$

Due to moiré lattice translation symmetry, the nodal positions of wave function $\Psi_{\mathbf{K},i}(\mathbf{r})$ can be increased by any integer multiple of the translation vectors $\mathbf{L}_{I/II}$. Hence, Eq.B20 and Eq.B24 can be written in uniform form with arbitrary integers n_I and n_{II}

$$a_i + a'_i = \frac{1}{3} + \frac{(\mathbf{k} - \mathbf{K}) \cdot \mathbf{L}_I}{2\pi} + n_I, \quad b_i + b'_i = \frac{2}{3} - \frac{(\mathbf{k} - \mathbf{K}) \cdot \mathbf{L}_{II}}{2\pi} + n_{II}, \quad (\text{B26})$$

Then, the uniform relation between nodal coordinates is

$$l_i + l'_i = \frac{1}{3} + \frac{(\mathbf{k} - \mathbf{K}) \cdot \mathbf{L}_{II}}{2\pi} + n_{II}, \quad m_i + m'_i = \frac{2}{3} - \frac{(\mathbf{k} - \mathbf{K}) \cdot \mathbf{L}_I}{2\pi} + n_I. \quad (\text{B27})$$

3. Evolution of nodes in real space

Here, we also calculate the nodal evolution along $\mathbf{K}'\mathbf{K}_1$ and $\mathbf{K}_1\mathbf{K}_3$ paths and flat band wave function at $\mathbf{k} = \mathbf{M}_3$ to confirm the validity of analytical expressions Eq.B19/B23 and Eq.B27 about wave functions and nodal coordinates. As the momentum \mathbf{k} varies along $\mathbf{K}'\mathbf{K}_1$ and $\mathbf{K}_1\mathbf{K}_3$ paths denoted by circles with green-yellow-red gradient color in Fig.8 (a), the evolutive coordinates of nodal points for the flat bands No.1/2 obey analytical expressions Eq.B27 in Fig.8 (b) and (c). At $\mathbf{k} = \mathbf{K}'$, the flat band wave function $\Psi_{\mathbf{k},1}$ has two nodal points at AA and AB_i ($i=1,2,3$), and $\Psi_{\mathbf{k},2}$ only has one nodal point at BA_i ($i=1,2,3$), where AB_2 , BA_1 and BA_3 are chosen as representative points. As \mathbf{k} moves from \mathbf{K}' to \mathbf{K}_1 , for flat band wave function $\Psi_{\mathbf{k},1}$, one nodal point moves continuously from AB_2 to AA, while the other moves from AA to BA_2 . Correspondingly, two nodal points of $\Psi_{\mathbf{k},2}$ move from BA_1/BA_3 to AB_3/AB_1 . With \mathbf{k} further varying along the $\mathbf{K}_1\mathbf{K}_3$ path, one nodal point of $\Psi_{\mathbf{k},1}$ moves from BA_2 to BA_1 while the other first moves away from AA and then returns, and two nodes of $\Psi_{\mathbf{k},2}$ move from AB_1/AB_3 to AB_3/AB_2 . In addition, we calculate the flat-band wave functions from Hamiltonian $H^\varphi(\mathbf{r})$ and Eq.B19/B23 at $\mathbf{k} = \mathbf{M}_3$, which are labelled in red squares and blue triangles in Fig.8 (d) and (e), and the good agreement between them verifies the validity of wave function from analytical expressions. In the following, we take $\mathbf{K} = \frac{1}{3}\mathbf{b}_I - \frac{2}{3}\mathbf{b}_{II}$, $\mathbf{M}_3 = \frac{1}{2}\mathbf{b}_I - \frac{1}{2}\mathbf{b}_{II}$ and $\mathbf{P} = 0.5\mathbf{b}_I - 0.3\mathbf{b}_{II}$ points as examples to check Eq.B27.

(1) At $\mathbf{k} = \mathbf{K}$, the Eq.B27 becomes

$$l_i + l'_i = \frac{1}{3} + \frac{(\mathbf{K} - \mathbf{K}) \cdot \mathbf{L}_{\text{II}}}{2\pi} + n_{\text{II}} = \frac{1}{3} + n_{\text{II}}, \quad m_i + m'_i = \frac{2}{3} - \frac{(\mathbf{K} - \mathbf{K}) \cdot \mathbf{L}_{\text{I}}}{2\pi} + n_{\text{I}} = \frac{2}{3} + n_{\text{I}}. \quad (\text{B28})$$

Since the two nodal positions of $\Psi_{\mathbf{K},1}(\mathbf{r})$ are located at AA and BA points with $\mathbf{r}_{AA} = 0$ and $\mathbf{r}_{BA} = \frac{\mathbf{L}_{\text{I}} + 2\mathbf{L}_{\text{II}}}{3}$, and the nodal position of $\Psi_{\mathbf{K},2}(\mathbf{r})$ is located at AB point with $\mathbf{r}_{AB} = \frac{-\mathbf{L}_{\text{I}} + \mathbf{L}_{\text{II}}}{3}$. Then, we can get

$$l_1 = 0, \quad m_1 = 0, \quad l'_1 = \frac{1}{3}, \quad m'_1 = \frac{2}{3} \quad \text{and} \quad l_2 = -\frac{1}{3}, \quad m_2 = \frac{1}{3}, \quad l'_2 = -\frac{1}{3}, \quad m'_2 = \frac{1}{3},$$

which satisfy Eq.B28 with $n_{\text{I}} = n_{\text{II}} = 0$ for flat band No.1, and with $n_{\text{I}} = -1$ and $n_{\text{II}} = 0$ for flat band No.2.

(2) At $\mathbf{k} = \mathbf{M}_3$, the Eq.B27 becomes

$$l_i + l'_i = \frac{1}{3} + \frac{(\mathbf{M}_3 - \mathbf{K}) \cdot \mathbf{L}_{\text{II}}}{2\pi} + n_{\text{II}} = \frac{1}{2} + n_{\text{II}}, \quad m_i + m'_i = \frac{2}{3} - \frac{(\mathbf{M}_3 - \mathbf{K}) \cdot \mathbf{L}_{\text{I}}}{2\pi} + n_{\text{I}} = \frac{1}{2} + n_{\text{I}}. \quad (\text{B29})$$

Because the two nodal positions of $\Psi_{\mathbf{M}_3,1}(\mathbf{r})$ ($\Psi_{\mathbf{M}_3,2}(\mathbf{r})$) are located at $AA(X_2)$ and $X_1(X_3)$ points with $\mathbf{r}_{AA} = 0$ ($\mathbf{r}_{X_2} = \frac{\mathbf{L}_{\text{II}}}{2}$) and $\mathbf{r}_{X_1} = \frac{\mathbf{L}_{\text{I}} + \mathbf{L}_{\text{II}}}{2}$ ($\mathbf{r}_{X_3} = \frac{\mathbf{L}_{\text{I}}}{2}$), then

$$l_1 = 0, \quad m_1 = 0, \quad l'_1 = \frac{1}{2}, \quad m'_1 = \frac{1}{2} \quad \text{and} \quad l_2 = 0, \quad m_2 = \frac{1}{2}, \quad l'_2 = \frac{1}{2}, \quad m'_2 = 0,$$

which satisfy Eq.B29 with $n_{\text{I}} = n_{\text{II}} = 0$ for flat band No.1/2.

(3) At $\mathbf{k} = \mathbf{P}$, the Eq.B27 becomes

$$l_i + l'_i = \frac{1}{3} + \frac{(\mathbf{P} - \mathbf{K}) \cdot \mathbf{L}_{\text{II}}}{2\pi} + n_{\text{II}} = 0.7 + n_{\text{II}}, \quad m_i + m'_i = \frac{2}{3} - \frac{(\mathbf{P} - \mathbf{K}) \cdot \mathbf{L}_{\text{I}}}{2\pi} + n_{\text{I}} = 0.5 + n_{\text{I}}. \quad (\text{B30})$$

Since the nodal points of wave functions for flat bands No.1/2 are $N_1 = -0.3265\mathbf{L}_1 - 0.5607\mathbf{L}_2$, $N'_1 = 0.0266\mathbf{L}_1 + 0.0612\mathbf{L}_2$, $N_2 = 0.236\mathbf{L}_1 - 0.2986\mathbf{L}_2$ and $N'_2 = -0.5358\mathbf{L}_1 - 0.201\mathbf{L}_2$, then we can get

$$l_1 = -0.3265, \quad m_1 = -0.5607, \quad l'_1 = 0.0266, \quad m'_1 = 0.0612 \quad \text{and} \quad l_2 = 0.236, \quad m_2 = -0.2986, \quad l'_2 = -0.5358, \quad m'_2 = -0.201,$$

which satisfy Eq.B30 with $n_{\text{I}} = n_{\text{II}} = -1$ for flat band No.1/2.

[1] Z.-D. Song, B. Lian, N. Regnault, and B. A. Bernevig, Phys. Rev. B 103, 205412 (2021).